Segmented Silicon-Micromachined Microelectromechanical Deformable Mirrors for Adaptive Optics

Adisorn Tuantranont and Victor M. Bright

Invited Paper

***Abstract*—Deformable mirrors improve optical efficiency of a system by correcting the wave front aberration caused by imperfections in the system components or by turbulent atmosphere in case of telescope optics. Micromachined mirror technology has the potential to substantially reduce the cost of adaptive optics systems. First, a brief review of the work in this field is presented with the goal of informing the reader of the challenges in the micromachined adaptive optics and the implementation tradeoffs including stress-induced curvature of multilayer mirrors. Then, recent results on the silicon micromachined, hybrid integrated microelectromechanical deformable mirrors for adaptive optics developed at the University of Colorado are presented. Various microfabrication processes including surface micromachining, bulk micromachining, and flip-chip assembly are implemented to fabricate high optical fill factor and large-stroke piston-type micromirror arrays. The achieved micromirror deflection for some designs is in the range of 2 to 3.5 μm, which results in the operating wavelength within infrared spectrum. Techniques to integrate microlenses on top of the micromirrors using self-aligned solder or transfer of ultrasmooth mirror plates on top of the micromirror actuators using flip-chip create high optical fill factor devices. Experimental results of aberration correction with such devices are presented.**

***Index Terms*—Aberration correction, adaptive optics, deformable mirror, infrared, MEMS, MOEMS, microlens, micromirror, optical MEMS.**

I. Introduction

A DEFORMABLE mirror is one of the core components in an adaptive optics system. Static optical wave front aberration in an optical system may occur due to the imperfections in the optical components. Dynamic wave front aberration occurs in telescope systems due to the turbulence of the earth's atmosphere. Thus, the performance of many optical systems may degrade by the presence of space and time varying optical wave front aberration. Astronomical and space surveillance telescopes are some of examples of the aberration-corrupted systems. The effect of aberration is to reduce the resolution of the image system by broadening the point spread function. One approach to improve the performance of these imaging systems is to apply the concept of adaptive optics to correct the aberration by using a deformable mirror which may be a segmented mirror or a continuous facesheet mirror. The ability to control the phase of a propagating optical wave front is a key enabling technology for improving the performance in many scientific, commercial, medical, and defense applications. By manipulating the wave front it is possible to correct aberrations in optical systems, control the shape of a focused laser beam, and redirect the laser beam. This leads to many scientific applications including real time active optical wave front control for correcting atmospheric turbulence effects for astronomy and space surveillance to provide higher resolution imagery, and control of fixed aberrations in optical systems to allow the development of simpler lens and mirror arrangements. Moreover, there are many possible commercial applications for optical wave front control that include beam steering for displays or scanners; aberration compensation in projection lithography systems; solid state device focus control for detectors and imagers; beam quality control for line-of-sight laser communications; optical interconnects between high speed electronic modules; and laser eye corrective surgery.

For miniature optical systems, microelectromechanical systems (MEMS) offer a cost effective device technology for manipulating the phase of a propagating optical wave front. Microfabricated deformable mirrors described in this paper are micromechanical devices that consist of a dense array of small, closely spaced reflective surfaces (micromirrors) whose vertical position can be electrically controlled. A lenslet array may be integrated directly over the array of micromirrors to increase the optical fill factor of the system. The gap between the micromirror and lenslet chips can be controlled precisely by microfabricated spacers or self-aligned solder techniques. The use of a lenslet to focus the incoming laser beam onto the reflective surface of a micromirror substantially increases optical fill factor of the overall hybrid microsystem, which in turn increases the optical efficiency and performance of the adaptive optics.

Manuscript received July 17, 2001; revised December 5, 2001. This work was supported by the Air Force Office of Scientific Research (AFOSR), Washington, DC, under Grant F49620-98-1-0291.

The authors are with the NSF Center for Advanced Manufacturing and Packaging of Microwave, Optical, and Digital Electronics, Department of Mechanical Engineering, University of Colorado, Boulder, CO 80309-0427 USA.

Publisher Item Identifier S 1077-260X(02)02219-0.

1077-260X/02$17.00 © 2002 IEEE

II. Micromachined Deformable Mirrors for Adaptive Optics

Conventionally manufactured deformable mirrors, continuous face sheet or segmented, have been successfully demonstrated and are being used in practical adaptive optics for correcting the atmospheric turbulence [1]. But the cost per channel of conventional deformable mirrors is still rather high due to the complex manufacturing processes that employ arrays of voice-coil actuators [2]. Recently, several attempts to construct deformable mirrors using microfabrication technologies have been demonstrated. For example, membrane-type mirrors using silicon bulk micromachining and wafer bonding techniques or surface micromachining have been demonstrated by the U.S. and Dutch researchers [3]–[6]. Membrane mirrors offer high optical efficiency with minimal diffractive effects, but suffer from complex control and actuation algorithms due to high mechanical cross talk between adjacent actuators. Segmented deformable mirrors offer an alternative approach with the highest degree of freedom and simplest control algorithms because each piston element can move completely independently. A disadvantage of a segmented deformable mirror is the somewhat low optical efficiency due to the gap between micromirror elements. A practical limitation of MEMS mirrors is the number of mirror elements in an array. Due to the need of addressing wires for each element and limited spacing between mirrors, the number of MEMS mirrors is limited to a maximum of a few hundred mirrors per array. Hybrid integration of MEMS mirror array on a complementary metal–oxide–semiconductor (CMOS) circuit chip or the use of CMOS switch integrated MEMS deformable mirrors (described in Section IV) are needed for implementing a very large micromirror array.

Another challenge frequently encountered with the micromachined mirrors is the mirror curvature induced due to multilayer material composition of the mirror plate (reflective metal on top of supporting polysilicon is a good example). An inherent characteristic of multilayer material MEMS structures is that misfit strains between the layers (due to intrinsic processing stresses or thermal expansion mismatch between the materials upon a temperature change) lead to stresses in the layers and deformation of the structure. Curvature measurements are routinely used in the microelectronics industry to determine stress states in metal films deposited on a substrate. Their attractiveness is based on the fact that wafer curvature can be easily and accurately measured, and through use of the Stoney (1909) formula (based on small-deformation linear elastic considerations), the measured curvature can be directly related to the film stress (which is typically biaxial and spatially uniform) without knowledge of the source of the stress or even the thermoelastic properties of the film. Much of the understanding regarding deformation of multilayers that has come from microelectronics applications is applicable to many MEMS applications, but significant differences exist and must be well understood for optimum and reliable MEMS design. In MEMS, the thicknesses of the layers are small (on the order of micrometer) and usually comparable. This leads to much larger deflections, relative to the thickness of structures, than are observed in microelectronics applications. For example, the maximum deflection of a 0.5-μm gold film on a 500-μm-thick 100-mm diameter silicon substrate subjected to a 100 °C temperature change is about two percent of the thickness. These values are not unrealistic for microelectronics applications. For MEMS applications, a reasonable example is a 0.5-μm gold film on a 1.5-μm-thick 400-μm diameter polysilicon plate. For this case, when subjected to a 100 °C temperature change, the maximum deflection is about six times the thickness. This can make it necessary to include geometric nonlinearity in order to accurately model deformation. Furthermore, the geometric nonlinearity can lead to bifurcations in the deformation behavior. These can be detrimental when dimensional stability is a requirement, or can be beneficial for actuator applications. Since the layers are of comparable thicknesses, stresses can vary appreciably through the thickness of the layers; the average stress in the layer may not be suitable to characterize film stresses as it is in many microelectronics applications. Tradeoffs between stress and curvature exist; for a given metal film thickness, decreasing the polysilicon thickness can reduce the stress in the metal, but at the expense of increasing the curvature. The significance of this is obvious as many MEMS applications (optical in particular) have strict deformation requirements, perhaps more severe than stress requirements. The curvature, and thus stresses, may vary significantly over the inplane dimensions of the structure; thus, the average curvature may be insufficient to adequately describe the deformation state of the structure.

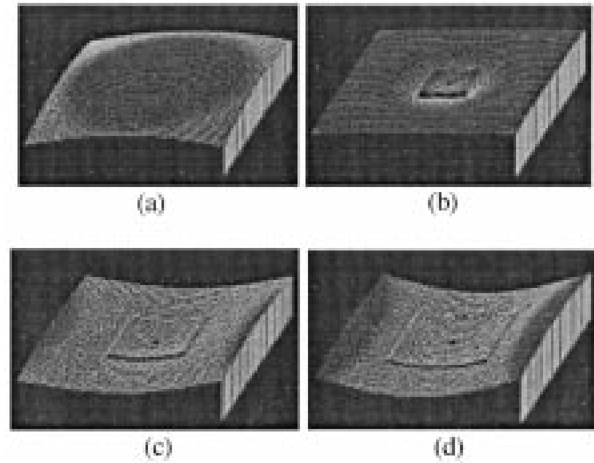

Fig. 1. Measured room temperature deformed shapes of polysilicon plate (450 μm × 450 μm) covered with a gold square pad ($L \times L$): a) $L = 0$ μm, b) $L = 100$ μm, c) $L = 150$ μm, d) $L = 200$ μm.

The patterning geometry of metal films on polysilicon (or other materials) may be arbitrary. This can result in complex spatially nonuniform deformation states. Fig. 1 shows measured deformed shapes for the polysilicon plates with square gold pads. Without a gold pad, there is a small roughly spherical deformation due to processing-induced intrinsic stresses. For the smallest gold pad, the deformed shape is also roughly spherical, corresponding to the shape that is predicted by a linear analysis. However, as the size of the gold pad is further increased, the deformed shape changes dramatically. For the two larger gold pads it is nearly cylindrical. Thus, the deformed shape, as a function of gold pad size, exhibits a bifurcation as the pad size increases. In this case, the deformed shapes exhibit a nearly cylindrical curvature. Fig. 2 shows similar measurement results for

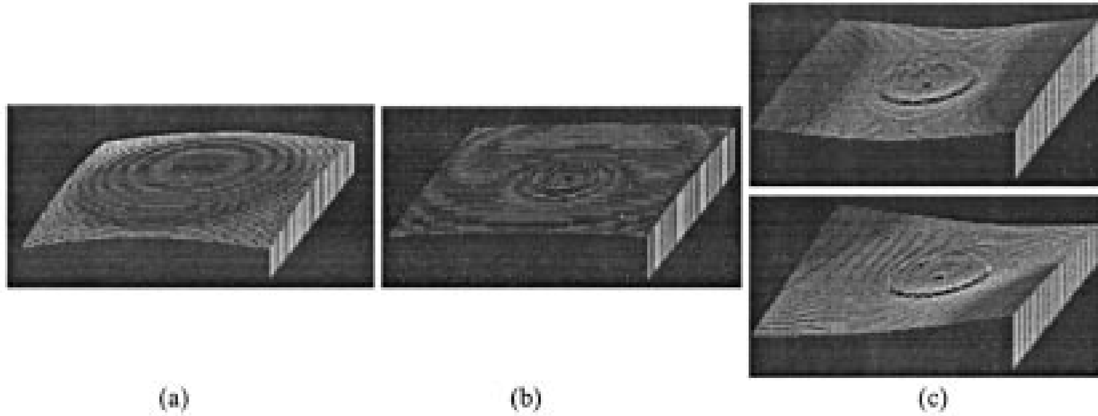

Fig. 2. Measured room temperature deformed shapes of polysilicon plate (450 μm × 450 μm) covered with a circular gold pad (D = diameter): a) $D = 0$ μm, b) $D = 100$ μm, c) $D = 150$ μm.

the polysilicon plates with circular gold pads. They too show a bifurcation from spherical to cylindrical curvature as the pad size increases. There appear to be two stable modes for the specimens with larger gold pad: a cylindrical mode deformed across the flats of the polysilicon plate, and a cylindrical mode deformed across the corners of the polysilicon plate. These deformed shapes cannot be predicted from linear theory and nonlinear analysis must be applied [7].

Segmented surface micromachined deformable mirrors have been reported previously for hexagonal and square mirror shapes [8]. Using electrostatic actuation, the mirror can be precisely position-controlled in the piston-type manner within one third of the gap between the top and bottom electrode. A tradeoff exists between the micromirror area, induced stress related curvature, and drive voltage. In order to lower the drive voltage one needs a large mirror. However, a large mirror has greater stress-induced curvature. A solution to this problem may be a large area mirror plate with a small reflective part in the center. A microlens can then be used to collect light and focus it on the reflective part of the mirror plate. A glass microlens array was manually aligned in front of the micromirror array to focus the incident light onto the reflective mirror surface. The demonstrated results showed ability of the device to correct spherical aberration in the visible spectrum [9]. The implementation of a lenslet integrated micromachined deformable mirror is still a challenge due to the lack of batch integration techniques of lenslets on micromirrors and the small mirror deflection achieved that is not adequate for modulating light in the infrared spectrum. In this paper, the development of novel hybrid integrated MEMS deformable mirrors is described. The devices include: a lenslet-integrated solder self-aligned surface micromachined mirror, CMOS bulk micromachined and lenslet integrated mirror, and the high-optical fill factor and large-stroke segmented micromirror fabricated through bulk micromachining of an actuator array hybrid integrated with piston-type mirror plates. The results of these novel MEMS deformable mirrors offer a low cost, high efficiency, and high-order wavefront correction ready to employ in adaptive optics systems including beam shaping and steering applications.

III. Surface-Micromachined MEMS Deformable Mirrors

A. Surface-Micromachined Deformable Mirror Description and Model

The surface micromachined deformable mirrors were designed at the University of Colorado and fabricated through the commercially available multiuser MEMS Process (MUMPs) that is a three-layer surface-micromachining polycrystalline silicon (polysilicon) process [10]. The device is comprised of 128 independent electrostatically controlled micromirror elements on a 12 × 12 square grid array (16 elements; four elements (2 × 2) in each corner are inactive for device evaluation purposes). The micromirrors are spaced on a 250-μm center-to-center grid to match the commercial refractive lenslet array from Nippon Sheet Glass Company [11]. Individual micromirror consists of a 3.5-μm-thick polysilicon plate (stacked POLY1 and POLY2 MUMP's layers) suspended by four flexures above a polysilicon (POLY0) drive electrode. The micromirror itself serves as the upper electrode and is electrically grounded. The flexures incorporate dimples to protect the mirror from electrically touching the drive electrode during the electrostatic snap through. The polysilicon support flexures are made out of POLY1 and are 12 μm wide, 155 μm long, and 2 μm thick. The nominal gap between the drive electrode and the micromirror is 2 μm (equal to the thickness of Oxide1 layer in MUMPs). The stacked polysilicon structure is used in the micromirror design, however beneath the metalized area of the mirror an additional oxide layer is inserted between the two polysilicon layers. This additional layer reinforces the mirror plate structure and reduces the surface curvature caused by the residual tensile stress in the gold metallization and compressive stress in the polysilicon layers. The reflective area of the mirror plate is covered by 0.5-μm- thick circle of gold 74 μm in diameter. Interferometric microscope measurement of the undeflected micromirror surface shows the curvature of less than 62 nm which is adequate for adaptive optics experiments at $\lambda_{\mathrm{HeNe}} = 632.8$ nm ($\approx\lambda/10$ optical flatness). Fig. 3 shows the scanning electron micrographs (SEMs) of an array of micromirrors. Each electrostatic mirror is individually

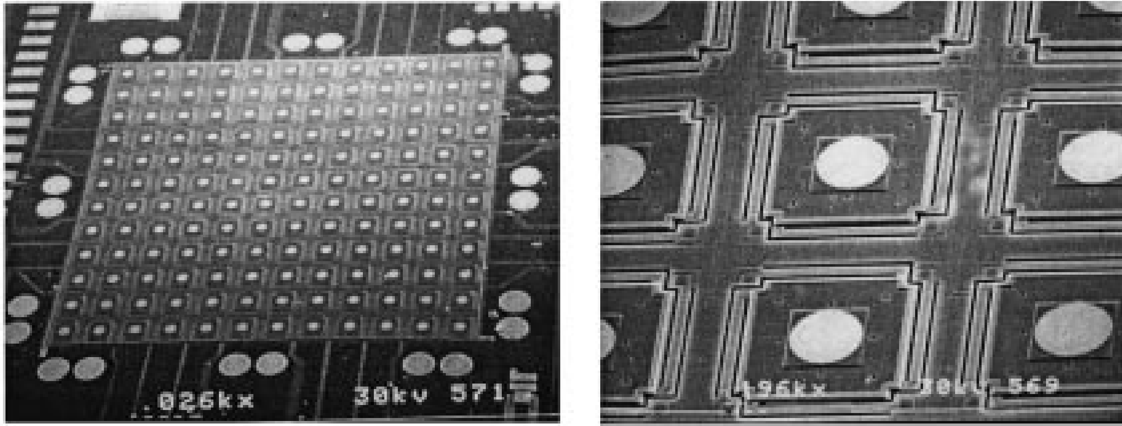

Fig. 3. Scanning electron micrographs of the array of surface micromachined micromirrors.

addressable via polysilicon (POLY0) wires that run under the support structure so that the topology induced in the overlying layers does not effected the flatness of the active mirror surfaces or the stiffness of the flexures. Electrostatic piston devices exhibit "snapthrough instability" behavior when deflection exceeds one third of the electrostatic gap [8], [9]. At this point, the linear restoring force of the flexures cannot counter the rapidly increasing nonlinear electrostatic force, and the micromirror is snapped onto the underlying electrode. The dimples on each flexure are designed to avoid destruction of the mirror by protecting the physical contact between the flexures and underlying electrode. By slowly increasing the applied voltage, while observing deflection on the interferometric microscope, the snap through voltage was measured for several mirror elements with the mean value of 11.4 V. The half-wavelength ($632/2 = 316$ nm) deflection voltage was measured approximately as 9.31 V [12]. This testing confirmed mirror device operation and provided the operating range of voltages used to generate mirror control voltages for the aberration correction experiments. From the observation on interferometric microscope, deflecting the micromirror toward the underlying drive electrode by applying an electrostatic potential produced no measurable change in the mirror curvature.

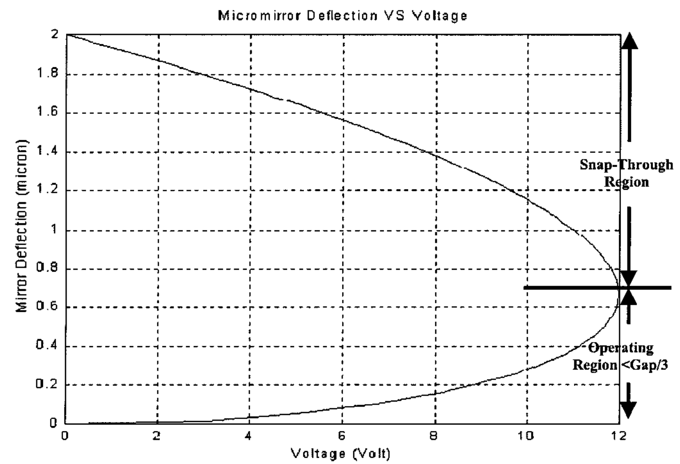

Fig. 4. Predicted applied voltage versus mirror deflection curve showing the operating and snap-through regions.

The spring constant of the micromirror flexures can be calculated analytically and is equal to 1.5×10^{-17} N/μm [13]. The area of the mirror is equal to 2.81×10^4 μm^2. Fig. 4 shows the analytical plot of applied voltage versus micromirror deflection using $k = 1.5 \times 10^{-17}$ N/μm. The plot shows the operating region which is about 1/3 of the electrostatic gap (from 0 to 0.7 μm) and snap-through region (from 0.7 to 2 μm).

The *CoSolve EM*, coupled electrostatic and mechanical solver, in MEMCAD software tool was used to produce a computer generated coupled electrostatic and mechanical solution of the micromirror [14]. The mirror plate is pulled down in response to the electrostatic force generated by the voltage potential difference applied at the electrodes. A 27-node brick scheme was used to mesh the mechanical structure of the device. By fixing the ends of all flexures, the voltage is applied across the electrostatic gap between electrodes filled with air and the mirror is free to move under electrostatic effect. Fig. 5 shows the modeled displacement of the micromirror under the 10-V bias. The mirror is pulled downward toward the drive electrode underneath. From the results of the MEMCAD model, the snap through voltage is 13 V, which is close to the experimentally obtained value of 11.4 V. Fig. 6 shows the plot of applied voltage versus mirror deflection for the analytical, MEMCAD simulation and experimental results. All the results are very close and prove the correctness of the model. The

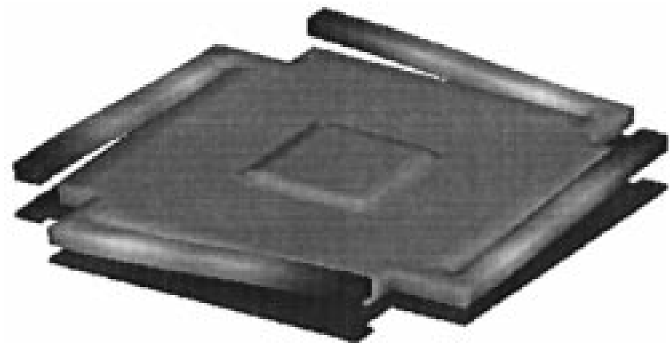

Fig. 5. Electrical–mechanical model using MEMCAD shows the displacement of the micromirror under 10-V bias.

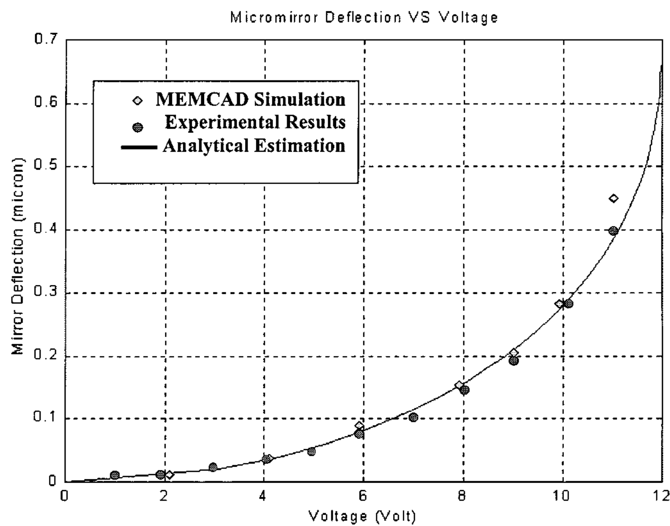

Fig. 6. Plot of the applied voltage versus mirror deflection for the analytical, MEMCAD simulation and experimental results.

mechanical resonance frequency of the micromirror was measured as 9.8 kHz [15].

B. Hybrid Integration of Lenslet Array With Surface-Micromachined Mirror

One way to greatly improve the effective fill factor with corresponding decrease in static background interference is to use a refractive lenslet array to focus the incident light beam onto only the reflective surface of the mirror [16]. The use of lenslet-integrated micromirror eases the micromirror design without specialized microfabrication process because the mirror surface can be small to reduce the stress-induced curvature and the requirement to control the underlying topography and planarization can be relaxed. The MEMS deformable mirror described here was designed specifically for use with an available commercial refractive planar type microlens array from Nippon Sheet Glass Company. Each lens has a circular shape of 250 μm in diameter. The 250-μm center-to-center spacing of the lens array matches with the center-to-center spacing of the micromirror array. The back focal length of the microlens is 560 μm. A hybrid flip-chip assembly was used to integrate the lenslet array above the micromirror array. Two glass spacers (540 μm thick and 1 mm $\times$ 3.5 mm) were first attached at the edges of the lenslet array glass chip with a UV curable epoxy. Then a 20-μm-thick UV curable epoxy layer was used to attach the spacers to the micromirror silicon chip. The lenslet array chip was optically aligned in lateral directions with the help of beam splitters. This technique allowed simultaneous view of the images of lenslet array and the micromirror array. The alignment was performed manually by adjusting the lateral position of the lenslet chip and rotation of the micromirror chip. The alignment is then verified under a interferometric microscope. Fringe patterns observed by the interferometric microscope are used to correct for tilt misalignment of the lenslet array chip. After the alignment, the lenslet array was fixed into place under UV light. The flip-chip assembly process is illustrated in Fig. 7. The gap between the microlens and micromirror is controlled by the spacer accurately and equals to the focal length of microlens with less than 5% error. The lenslet array integrated micromirror (shown in Fig. 8) is packaged into a 144 Pin Grid Array (PGA) using conductive epoxy and electrically connected to package by wire bonding. The device can, thus, be fabricated and packaged as a rugged,

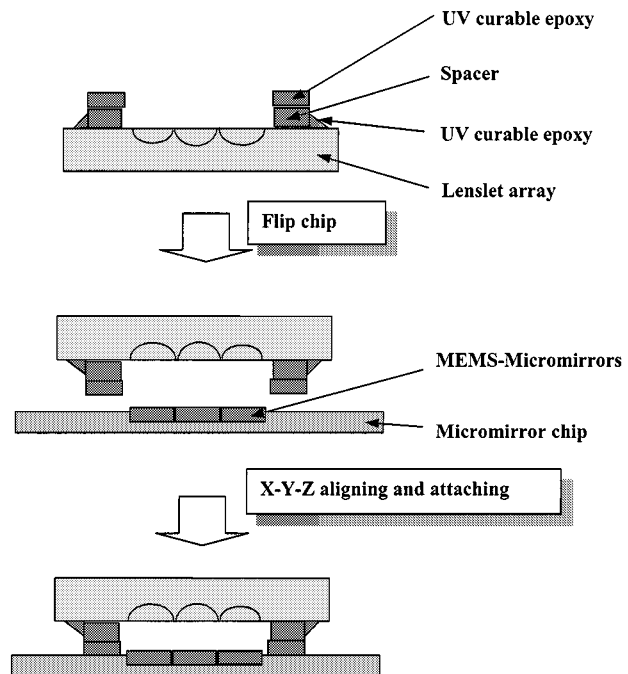

Fig. 7. Flip-chip assembly of the glass lenslet array on top of the micromirror array.

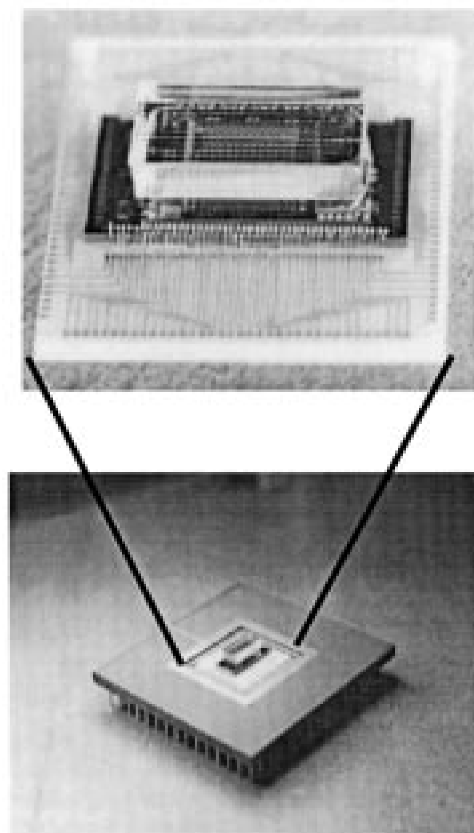

Fig. 8. The lenslet integrated micromirror attached and wire bonded to the fan-out ceramic substrate and the final device packaged in a 144 PGA.

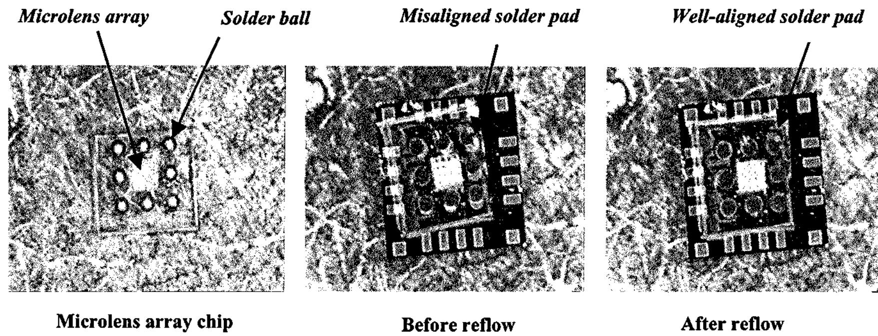

Fig. 9. The microlens chip with solder balls before assembly, the microlens chip on top of the micromirror chip before solder reflow and after solder reflow.

compact optical microsystem suitable for beam steering, beam shaping, and aberration correction applications. The results of the adaptive optics experiment are described in Section VI.

C. Advanced Lenslet Integration by Self-Aligned Assembly

The method described above involves integration of the lenslet array above the micromirror by flip-chip assembly with manual alignment. This method of integration is not suitable for batch fabrication due to its slowness and inadequate alignment accuracy. A self-aligned soldering technology can be used as an alternative, which may lead to batch fabrication of such devices. Self-aligned assembly using solder is often used in optoelectronics packaging [17]. It is a well-understood technology that can be adapted to integrate a lenslet array with micromirror without manual alignment and with high accuracy. The self-aligned soldering offers advantages of low cost, high yield, batch assembly, and self-aligning capability. In this technique, the surface tension force of molten solder drives the misaligned solder joint to become a well-aligned joint with minimum surface energy. The alignment occurs automatically during the solder reflow. The focal point of a lenslet can be aligned on the center of the micromirror reflective surface within submicrometer lateral alignment accuracy. A gap between the micromirror chip and the lenslet chip can be controlled precisely by the final height of the solder joint to be exactly the focal length of the microlens.

The solder joints for the device described in this paper were designed with assistance of a public domain software *Surface Evolver [18]* that was adapted to model reflow of molten solder. The software calculates solder shape with minimum surface energy [19]. Thus, the solder shape and the final gap between microlens chip and micromirror chip are defined by the surface energy minimization of molten solder bumps. The assembly parameters that have to be considered are bump height, solder volume, solder pad size, and number of solder pads. The device in this paper utilized a polymer microlens array with focal length of 122 μm [20]. To obtain the final joint height of 122 μm after solder reflow, the volume of each solder ball has to be 4.39 $\times$ 10^{-6} cm^3 according to the numerical calculation from the surface evolver [20]. The actual solder balls used in the device assembly were 8 ml in diameter. Eight solder pads of 190 μm in diameter were fabricated on the lenslet array chip to match the solder pads on the micromirrors chip. The solder pads were designed to support the weight of the lenslet array chip. The solder used was eutectic 63Sn/37Pb shaped in spheres of 0.008 in diameter with the diameter tolerance of $\pm$0.001 in. First, the solder balls were reflowed on the solder pads at 180 °C in a chamber filled with nitrogen and formic acid. Then the lenslet chip was flipped and placed on the micromirror chip. The assembly was then reflowed again in the chamber at 180 °C. After alignment, the chip was cooled down to lock the assembly. Fig. 9 shows the sequence of self-aligned soldering assembly. The lenslet array integrated micromirror chip was packaged into a 24 PGA using conductive epoxy and electrically connected to the package by wire bonding as shown in Fig. 10. The gap between the microlens chip and the micromirror chip was measured as 122 $\pm$ 1 μm and agrees well with the required gap of 122 μm [20]. The gap height misalignment is less than 1% of the predicted final gap height. The error occurred due to the variation in the solder volume ($\pm$0.001 in tolerance in diameter). The success of this solder assembly leads to possibilities of low-cost batch produced optical MEMS.

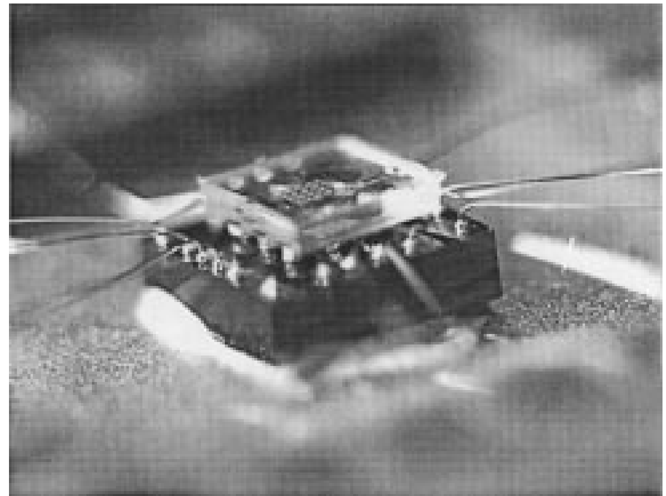

Fig. 10. The micromirror chip integrated with the lenslet array chip and attached and wire bonded to a package.

IV. CMOS MEMS DEFORMABLE MIRROR

Micromirrors with large deflections are required to modulate light in infrared spectrum. Most attempts at MEMS deformable mirrors use surface micromachining to fabricate parallel plate structures for electrostatically driven segmented or continuous-membrane deformable mirrors [6], [9], [12], [13].

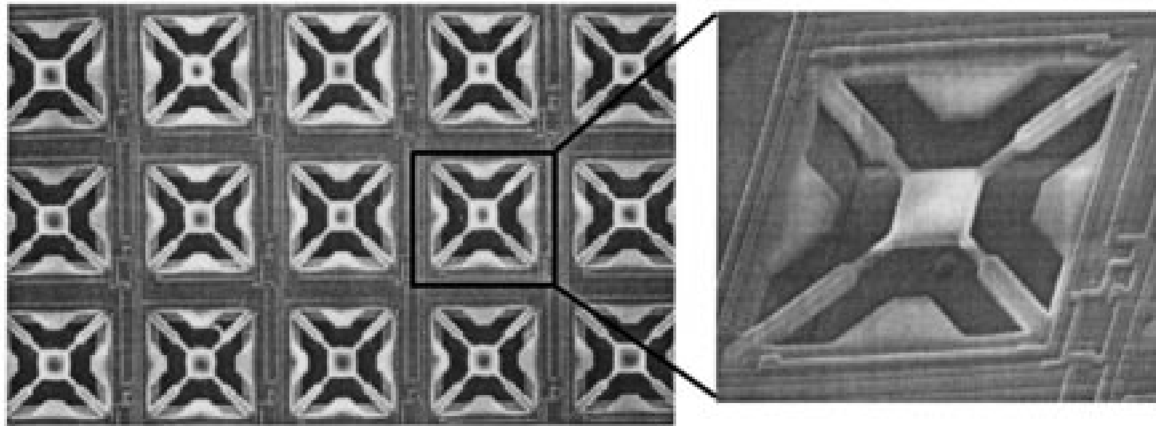

Fig. 11. CMOS phase-only modulation micromirror array.

Due to a narrow gap between the electrodes in a surface micromachined process, the mirror's deflection achieved is typically in the range of submicrometer unless a structure elevation method is used to raise the mirror above the substrate, thus, increasing the gap [21]. These attempts are not adequate to modulate light in longer wavelength than visible spectrum or are very difficult to implement in a batch-production process. Bulk micromachined mirror is a promising alternative technique to solve this limitation. The use of industrial CMOS technology enables the cointegration of mechanical microstructures with integrated circuits on the same chip. A MEMS deformable mirror, which is smarter and more concise, can be achieved by integration of digital or analog signal amplifying and processing integrated circuits right next to the micromirrors.

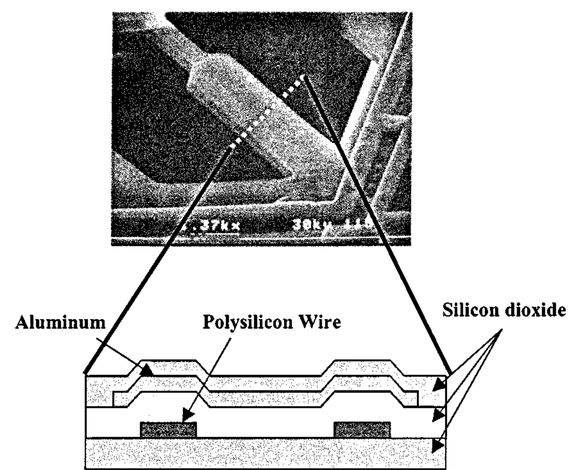

Fig. 12. Cross section of thermal multimorph actuator structure.

A. CMOS Micromirror Device Description

A two-dimensional (2-D) array of deflectable micromirrors (Fig. 11) was fabricated through the Orbit 2-μm double polysilicon, double metal CMOS process, provided by the MOS Implementation Service (MOSIS) [22]. The deformable mirror is designed to modulate light in the visible to near-infrared wavelengths by piston-type movement of its pixel elements (referred to as micromirrors). The individual micromirror consists of a 40 μm $\times$ 40 μm trampoline-type plate suspended by thermal multimorph flexures at each corner. The suspended plate is composed of stacked aluminum commonly available in standard integrated circuit processes. The aluminum optical reflectivity is greater than 90% over the operation wavelengths. The micromirror plate and multimorph actuators (flexures) are coupled with an oxide spring beam. The thermal multimorph structures consist of polysilicon resistor wires and aluminum layers encapsulated in silicon oxide, as shown in Fig. 12.

Due to the different coefficients of thermal expansion of multilayer sandwich of different materials, the actuators curl when an ohmic heating from the input electrical power is applied [23]–[25], thus causing piston-type motion of the micromirror plate. The array is anisotropically etched in ethylene diamine pyrochatechol (EDP) solution to release the micromirror structure from the surrounding substrate. A pit is formed under the suspended plate and actuator, giving high degree of thermal isolation from the substrate and minimizing the thermal crosstalk between elements. Piezoresistive deflection sensors are embedded at the base of flexures to provide real-time feedback control of the position of each micromirror. A CMOS switching circuit is integrated adjacent to each pixel to control current into the pixel actuators providing a row and column addressability of the array. The switching circuit allows digital addressing of the pixel by 5-V data pulses. The multi-morph actuator beam is 72 μm long, 14 μm wide, and 4.175 μm thick with 2.8 μm wide, 0.4 μm thick, and 150 μm long polysilicon heater wire running between the aluminum and oxide layers to generate heat. The ends of multimorph actuator beams are coupled to the micromirror plate with the oxide beams (21 μm long, 7 μm wide, and 3 μm thick). The flatness of the micromirror plate was measured with an interferometric microscope. The peak-to-valley deformation of the unactuated micromirror plate is 0.22 μm ($\approx\lambda/20$ of maximum operating wavelength of 4 μm). The deformation of the plate does not significantly change during actuation.

B. Finite-Element Model of CMOS Micromirror

A finite-element model was constructed to analyze the micromirror static deflection. The simulation of the micromirror was conducted with a commercially available finite-element analysis tool (MARC) [26]. The simulation consists of an

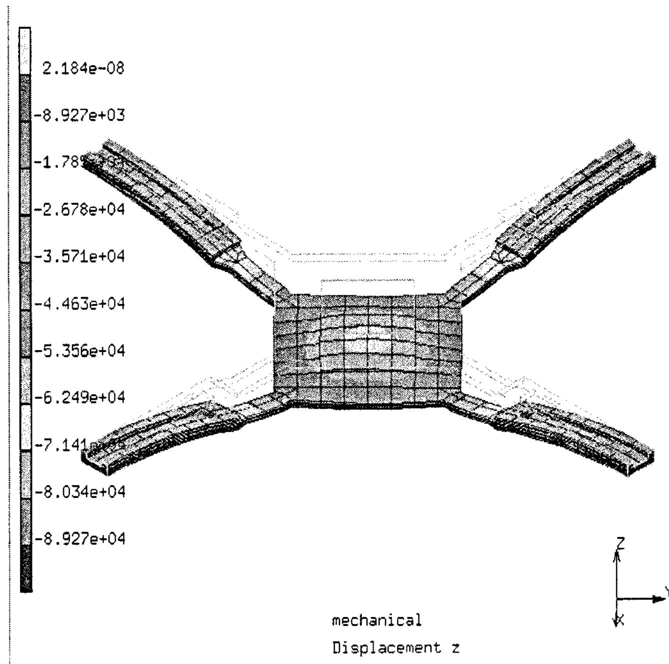

Fig. 13. FEM result showing the deflection of the CMOS micromirror. The input voltage was 8 V and the vertical axis is 0.6 μm

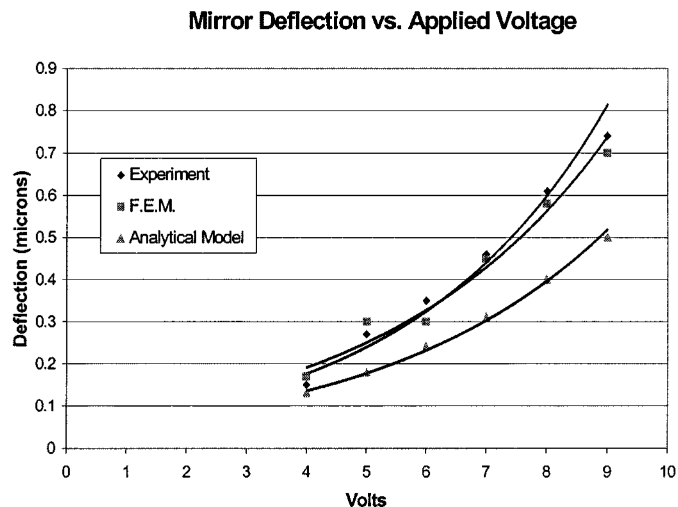

Fig. 14. Mirror deflections obtained from the analytical model, the finite-element model, and the experimental results in operating voltage range from 4 to 10 V.

electrothermal analysis to obtain the temperature distribution resulting from an input electric power. This is then coupled to a thermal–mechanical analysis in which the temperature distribution is used to determine deflections resulting from the thermal expansion mismatch in a multimorph structure. The simulated micromirror deforms as shown in Fig. 13.

C. CMOS Micromirror Characterization

Fig. 14 shows the mirror deflection versus applied voltage for the analytical model, finite-element model, and the experimental measurement. The deflection measurements were obtained with an interferometric microscope at the center of the micromirror plate. The experimentally determined mirror deflection versus applied power is shown in Fig. 15. The mirror deflection depends linearly on the drive power with the maximum power of 150 mW per pixel at 2-μm deflection with nonlinear effect near zero due to the buckling of the heated beam. There is no tilting of the actuated micromirror as observed from both simulation and experimental results. Deflection of the micromirror is detected with two piezoresistors embedded in the opposing beams at the clamped edges of the beams, where the mechanical stress is highest. The measured change in resistance in a single piezoresistor related to the mirror deflection as a linear relation is shown in Fig. 16. Dynamic measurements were also taken to determine the maximum operating frequency of the micromirror. A laser interferometer was used to determine the time required to heat and cool the multimorph beams. The maximum controllable operating frequency of 100 Hz was achieved [27]. To increase the optical fill factor of the entire device, a microlens array can be integrated directly above the micromirrors. The concept is similar to the lenslet integrated surface micromachined device described earlier. Fig. 17 shows the final lenslet integrated CMOS micromirror array packaged in a 40 pins package [28]. The lenslet array is the same glass microlens array as for the device depicted in Fig. 8.

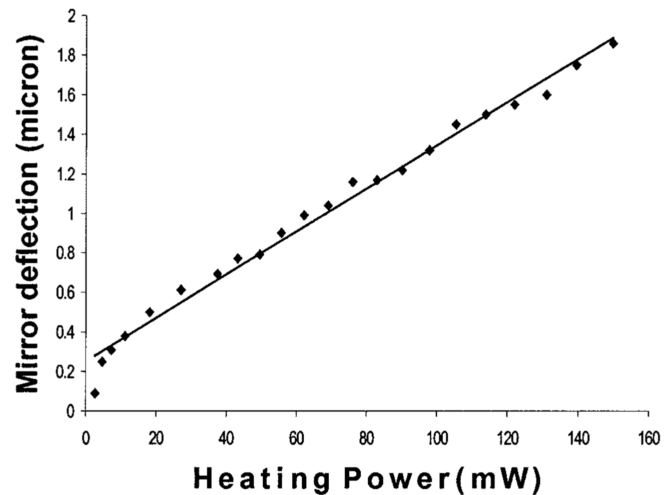

Fig. 15. Plot of CMOS micromirror deflection as a function of heating power.

Fig. 16. Plot of CMOS micromirror deflection as a function of relative change in resistance of a single piezoresistor.

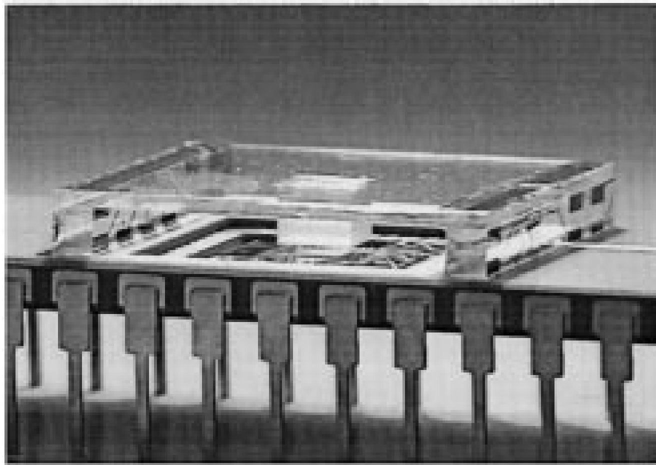

Fig. 17. The lenslet array flip-chip integrated on top of the CMOS micromirror array using glass spacers for gap control and packaged in a 40 pin package.

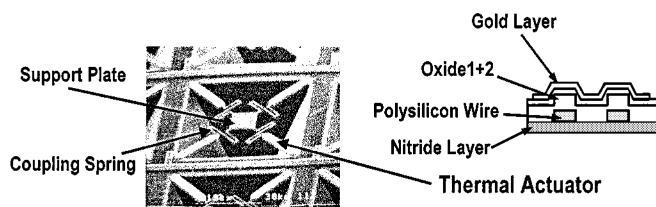

Fig. 18. A MUMP's bulk-micromachined microactuator consists of four thermal multimorph actuators coupled to a central polysilicon plate.

V. Surface Micromachined and Bulk-Etched MEMS Deformable Mirror

A novel technique, bulk underetched surface micromachining using MUMPs, that combines the surface and bulk micromachining can be used to implement a micromirror array that operates in wavelength spectrum extending into infrared. Moreover, to increase the optical fill factor of the array, flip-chip MUMPs on MUMP's process may be used to integrate polysilicon micromirror plates on top of the MEMS actuators. Thus, extremely high optical fill factor (>98%) deformable micromirror is possible without using microlens arrays.

A. Bulk-Etched MUMP's Micromirror Description

The 2-D array of deflectable micromirrors begins with fabrication of the actuators through the MUMP's technology. The individual MEMS actuator pixel consists of a 40 μm $\times$ 40 μm trampoline-type polysilicon plate suspended by thermal bimorph actuators at each corner, as shown in Fig. 18. The thermal actuator consists of the layer of Oxide 1 and Oxide 2 between the gold and Poly0 wire. The central polysilicon plate and bimorph actuators are coupled with a folded spring oxide beam of 5 μm in width, 2.75 μm in thickness, and 100 μm in length. The pit opening for the pixel is the square shape and has dimensions of 200 μm $\times$ 200 μm. The center-to-center spacing of the pixels is 250 μm in both X and Y directions. EDP is used to etch the crystal silicon substrate underneath the suspended structures. In addition, a flip-chip transfer technique is used to integrate 248 μm $\times$ 248 μm polysilicon micromirror plates with 2-μm spacing between the mirrors on top of the actuator array. The micromirror plates are also fabricated through MUMPs, but on a separate chip. The micromirror plate consists of the layers of gold on polysilicon or trapped oxide structure (oxide trapped between the Poly1 and Poly2 layers) to increase the mirror plate thickness and reduce the stress-induced curvature. The flip-chip assembly results in a micromirror array of very high optical fill factor (≈98%). Gold or solder bumps can be used to bond the actuator array and polysilicon mirror plates together. The bonded structure is then released in a hydrofluoric acid rinse to remove the silicon substrate from the micromirror plates and free the actuator structures [29]. The array is then anisotropically etched in EDP solution to form truncated pyramidal pits under the suspended actuator structures, giving high degree of thermal isolation from the surrounding substrate. An array of micromirrors that was flip-chip transferred onto the actuator array is shown in Fig. 19, one mirror in the lower right corner is removed to display the actuator structure.

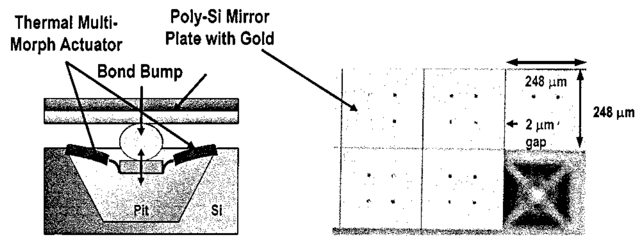

Fig. 19. The MUMP's fabricated flip-chip assembled and bulk underetched micromirror array.

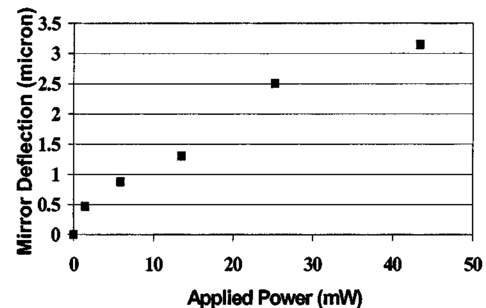

Fig. 20. MUMP's bulk micromachined micromirror deflection as a function of applied power.

B. Bulk-Etched MUMP's Micromirror Characterization

The maximum deflection of the assembled micromirror was measured under an interferometric microscope. The deflection of the micromirror as a function of applied electrical power is shown in Fig. 20. Deflection measurements were taken at the center of the micromirror. The mirror deflection depends linearly on the drive power with maximum deflection of 3 μm at 45 mW of applied power. Thus, the maximum operating wavelength of this device is 6 μm. The peak to valley deformation of the mirror is less than 400 nm or about λ/15 of the maximum operating wavelength. The maximum operating frequency of the device was measured as 2.7 kHz [30].

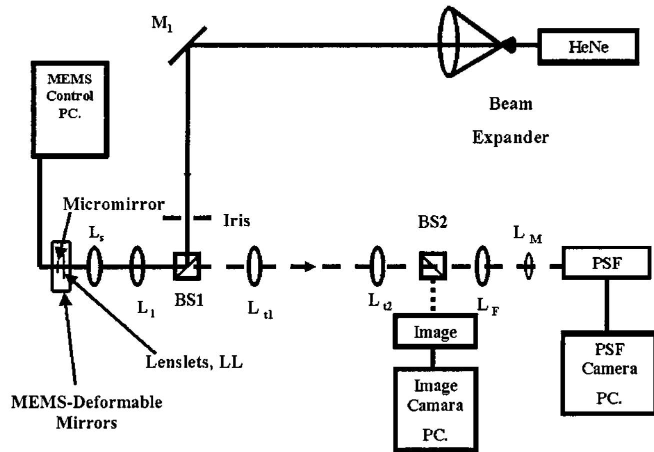

Fig. 21. The optical experimental setup for measuring the far-field diffraction pattern of tested MEMS deformable mirrors.

VI. Adaptive Optics Experiment and Results

A. Experimental Setup

To illustrate the type of results possible with a segmented piston-type micromirror array, consider the surface-micro-macined and lenslet integrated array described in Section III. The observation of the far-field diffraction pattern obtained from the reflection of a coherent beam off the deformable mirror surface is the best method to determine the quality of the mirror. The measured zeroth-order (on-axis) intensity of the far-field diffraction or point spread function (PSF) is a function of the mirror surface quality and array fill factor. The optical experimental setup shown in Fig. 21 was used to measure the far-field diffraction pattern of the tested MEMS deformable mirrors. The collimated 18-mW Helium–Neon (HeNe) laser (wavelength $=$ 632.8 nm) was used as a signal light source. The collimated beam is passed through the spatial filter to obtain a clean light signal and expanded beam. The beam is folded by mirror M_1 into the optical characterization branch. The beam enters a beam splitter (BS1) and is redirected toward the MEMS mirror by passing through a pair of lenses L_l and L_s between BS1 and the MEMS mirror. This pair of lenses serves to reduce the diameter of beam to fill the controllable mirror surface of the tested device. The packaged MEMS mirror is mounted in the test bench and located at the back focal plane of lens L_s. An iris is located in front of BS1 a focal length away from lens L_l to control beam diameter. The modified beam from the MEMS mirror is reflected back through the afocal telescope (L_l and L_s), BS1 and translating lenses L_{t1} and L_{t2}. The beam enters a Fourier transforming lens L_F and generates the far-field diffraction. A 256 $\times$ 256 pixel CCD camera is used to capture the image of the far-field diffraction pattern. Focal lengths of lenses and specification of optical component locations in the experimental setup are shown in Tables I and II [12]. Insertion loss of MEMS mirror is small (<1 dB) due to the high reflectivity of mirror surface (>95%) and high transmission of microlens array (>90%).

The reflected wavefront (far-field diffraction pattern) from the bare micromirror array (no lenslets) and the lenslet-integrated device with self-aligned solder assembled lenslets was measured and is shown in Fig. 22. The far-field diffraction pattern of the lenslet-integrated device is obviously clearer compared to that of the bare micromirror array. The static background interference is reduced. The unwanted far-field diffraction pattern located around the central lobe and the blur in the higher order lobes is reduced.

TABLE I
Focal Lengths of Lenses Used in the Experimental Setup

Lens	Focal length (mm)
L_l	250
L_s	500
LL	0.56
L_{t1}, L_{t2}	300
L_F	75.6
L_M	12.7

TABLE II
Specifications of Optical Component Locations in the Experimental Setup

Distance	Nominal Distance (mm)
Iris to L_l	250
L_l to L_s	750
L_s to LL	500
LL to micromirror	0.56
L_l to L_{t1}	550
L_{t1} to L_{t2}	600
L_{t2} to L_F	375.6
L_F to L_M	75.6
L_M to CCD camera	90

B. Aberration Correction Experimental Results

The experiment is setup to demonstrate aberration correction ability by performing focus/defocus of the signal beam. It is demonstrated that the reconstructed, aberration corrected wavefront compared to the aberrated wavefront is greatly improved in main lobe intensity and full-width at half-maximum (FWHM).

1) Unaberrated Beam Profile: The 12 $\times$ 12 micromirrors were wired into six circular rings and were first driven by the same voltage applied to each ring. In this case, the mirror array was deformed uniformly as the plane mirror without an induced aberration from MEMS mirrors. No aberration was applied to the system. The input laser power of 1.2 μW was measured right behind the first iris and the neutral density filter (ND filter) was used to adjust the intensity of the signal beam. Fig. 23(a) shows the profile of the beam from central line scan of CCD camera. The central (zeroth-order) lobe and the first order lobe of diffracted beam are measured on upper graph and the PSF of the central diffraction order is shown on the lower graph. The FWHM of diffraction pattern is measured equal to 4.26 μs and the peak intensity of the central lobe is 1.402 mV. The relative

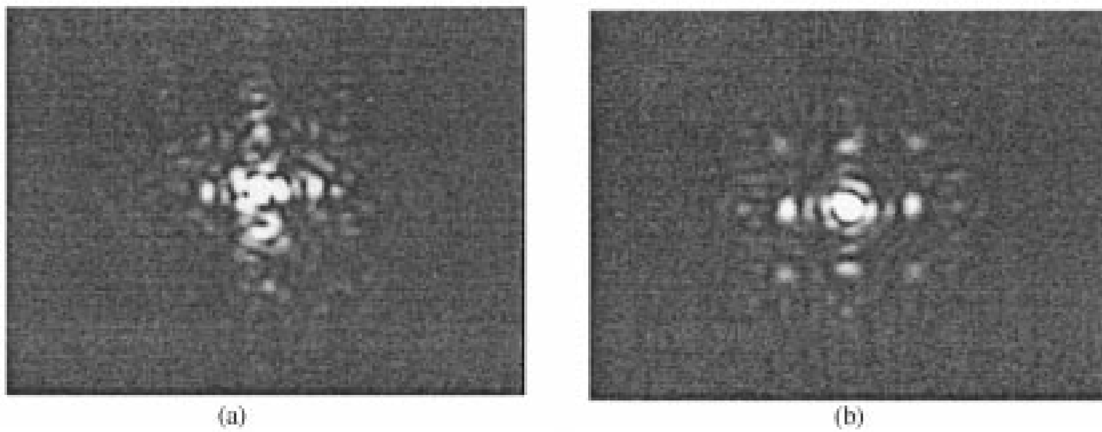

Fig. 22. The far-field diffraction pattern in the vicinity of zeroth-order of (a) bare micromirror array and of (b) the lenslet-integrated MEMS mirror.

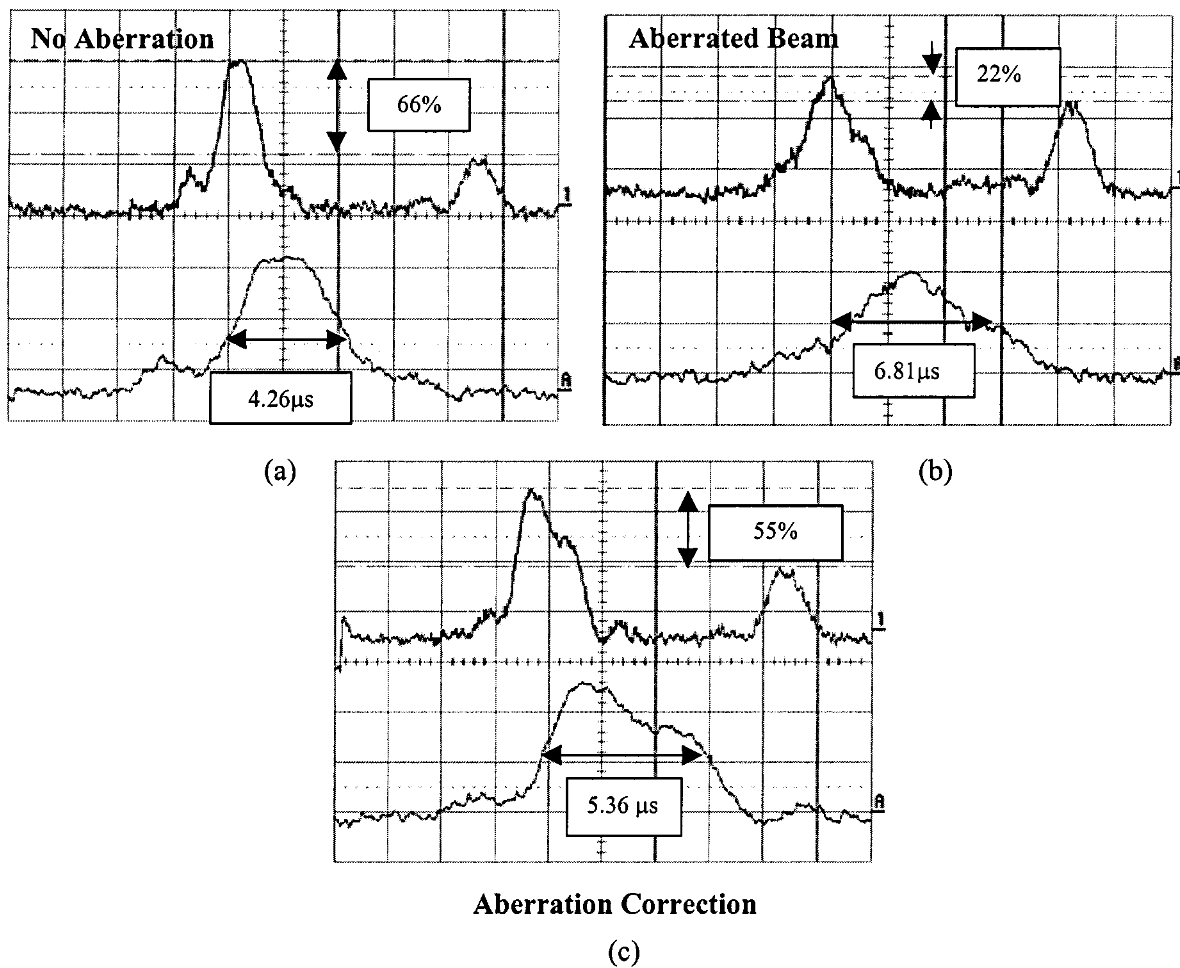

Fig. 23. Beam profiles of the central (zeroth-order) lobe and the first-ordered lobe (upper trace) and the FWHM of the main central lobe (lower trace) of the (a) unaberrated beam, (b) aberrated beam, and (c) aberration corrected beam.

peak intensity of the central lobe to the first order lobe is 922 mV (=66%).

2) Aberrated Beam Profile: To introduce aberration into the experimental optical system, a lens with $f = -500$ was inserted into the system at the distance 1700 mm from the first iris to generate the aberration radius of curvature 3500 mm onto the MEMS deformable mirror. The amount of input light into the system was reduced significantly due to the spreading of light when the light is aberrated. The power of input light was measured and controlled to be equal to 1.2 μW (the same amount of power as in the case of no applied aberration). Fig. 23(b) shows the diffraction pattern of aberrated beam reflected from the MEMS deformable mirror (the mirror is not deformed and no aberration correction has been performed). The effect of the aberration is the loss in peak intensity and the associated increase in off-center intensity when the aberrated wavefront is

reflected from the undeformed MEMS mirror. As shown in the beam profile in Fig. 23(b), the peak intensity is reduced to 1.1 mV and the relative peak intensity of the central lobe to the first order lobe is also reduced to 242 mV (=22%). The defocus of light affects power of light in the central lobe spread as seen in the increase of FWHM of main lobe to 6.81 μs (60% increment from original FWHM).

3) Corrected Beam Profile: A series of voltages was applied to the MEMS deformable mirror in order to correct the reflected aberrated wavefront. The measured PSF associated with the reflection of the aberration corrected wavefront from the deformed MEMS mirror resulted in the diffraction pattern and beam profile presented in Fig. 23(c). The improvement in the PSF is primarily evident in the greater central lobe peak intensity of corrected PSF when the MEMS deformable mirror is used to correct the aberration. The FWHM of central lobe is reduced to 5.36 μs, which is approximately 21% reduction from the uncorrected case. The relative peak intensity of central lobe to the first order lobe is increased to 773 mV (=55%) which is approximately two and a half times improvement as compared to the relative peak intensity in the case of aberrated wavefront. It should also be noted that the off-axis intensities decreased as a result of correction. These results indicate that the tested MEMS deformable mirror can be used as an aberration corrector in an adaptive optics system.

VII. Conclusion

Micromachined deformable mirrors offer a low-cost adaptive optics solution. In this paper, several silicon micromachined and hybrid integrated deformable mirrors for adaptive optics have been demonstrated. In particular, high optical fill factor and large-stroke piston-type micromirror arrays can be fabricated using surface micromachining, flip-chip assembly, and bulk micromachining techniques. With large mirror deflection achieved, the MEMS deformable mirrors can be used for phase modulation of light from visible to infrared spectrum with moderate to high speed. Device configuration, modeling, and characterization have been described for the fabricated MEMS mirrors. Techniques to transfer ultrasmooth mirror plates on top of the micromirror actuator array using flip-chip transfer and integration of the lenslet array with the MEMS mirror array using self-aligned solder to create the high optical fill factor devices has been described. Experimental results of focus/defocus correction have been demonstrated to exhibit the ability of the MEMS deformable mirrors to correct optical wavefront aberrations.

References

[1] R. K. Tyson, *Principles of Adaptive Optics*, 2nd ed. New York: Academic, 1998, pp. 208–228.

[2] T. K. Barrett, D. G. Bruns, T. J. Brinkley, D. G. Sandler, B. C. FitzPatrick, J. R. P. Angel, and T. Rhoadarmer, “Adaptive secondary mirror for the 6.5-m MMT,” *Proc. SPIE*, vol. 3353, pp. 754–763, 1998.

[3] L. M. Miller, M. L. Agronin, R. K. Bartman, W. J. Kaiser, T. W. Kenny, R. L. Norton, and E. C. Vote, “Fabrication and characterization of a micromachined deformable mirror for adaptive optics applications,” *Proc. SPIE*, vol. 1945, pp. 421–430, 1993.

[4] J. D. Mansell, P. B. Catrysse, E. K. Gustafson, and R. L. Byer, “Silicon deformable mirrors and CMOS-based wavefront sensors,” *Proc. SPIE*, vol. 4124, pp. 15–25, 2000.

[5] G. Vdovin, S. Middlehoek, and L. Sarro, “Technology and applications of micromachined silicon adaptive mirrors,” *Opt. Eng.*, vol. 36, pp. 1382–1390, May 1997.

[6] T. G. Bifano, R. K. Mali, J. K. Dorton, J. Perreault, N. Vandelli, M. N. Horenstein, and D. A. Castanon, “Continuous-membrane surface micromachined silicon deformable mirror,” *Opt. Eng.*, vol. 36, pp. 1354–1360, May 1997.

[7] M. L. Dunn, Y. Zhang, and V. M. Bright, “Deformation and stability of gold/polysilicon layered MEMS plate structures subjected to thermal loading,” in *Mechanical Properties of Structural Films, ASTM STP 1413*: American Society for Testing and Materials, May 1, 2001. [Online]. Available: www.astm.org/STP/1413/1413_07.

[8] M. C. Roggemann, V. M. Bright, B. M. Welsh, S. R. Hick, P. C. Roberts, W. D. Cowan, and J. H. Comtois, “Use of micro-electro-mechanical deformable mirrors to control aberrations in optical systems: Theoretical and experimental results,” *Opt. Eng.*, vol. 36, pp. 1326–1338, May 1997.

[9] W. D. Cowan, M. K. Lee, B. M. Welsh, V. M. Bright, and M. C. Roggemann, “Surface micromachined segmented mirrors for adaptive optics,” *IEEE J. Select. Topics Quantum Electron.*, vol. 5, Jan./Feb. 1999.

[10] D. A. Koester, R. Mahadevan, and K. W. Markus, “Multi-user MEMS processes (MUMP’s): Introduction and design rules, rev.4,” MCNC MEMS Technical Applications Center, Research Triangle Park, NC, Technical Report, 1996.

[11] R. D. Myers, *Planar Microlens Array (PML): Preliminary Specifications*: NSG America, INC., 1998.

[12] A. Tuantranont, V. M. Bright, W. Zhang, and Y. C. Lee, “Flip chip integration of lenslet arrays on segmented deformable micromirrors,” *Proc. SPIE*, vol. 3680, pp. 668–678, 1999.

[13] ——, “Packaging of lenslet array on micromirrors,” *Proc. SPIE*, vol. 3631, pp. 156–164, 1999.

[14] *MEMCAD 4: User Handbook Revision 48.3*. Cary, NC: Microcosm Technologies, Inc., June 2000.

[15] T. Weyrauch, M. A. Vorontsov, T. G. Bifano, A. Tuantranont, and V. M. Bright, “Performance evaluation of micromachined mirror arrays for adaptive optics,” *Proc. SPIE*, vol. 4124, pp. 32–41, 2000.

[16] E. A. Watson, D. T. Miller, and K. J. Barnard, “Analysis of fill factor improvement using microlens arrays,” *Proc. SPIE*, vol. 3276, pp. 123–134, 1998.

[17] W. Lin, S. K. Patra, and Y. C. Lee, “Design of solder joints for self-aligned optoelectronic assemblies,” *IEEE Trans. Components, Packaging, and Manufacturing Technol.*, vol. 18, pp. 543–551, Aug. 1995.

[18] K. A. Brakke, *Surface Evolver Manual*: version 1.94, Geometry Center, Univ. Minnesota, 1994.

[19] K. Harsh and Y. C. Lee, “Modeling for solder self-assembled MEMS,” *Proc. SPIE*, vol. 3289, pp. 177–184, 1998.

[20] A. Tuantranont, V. M. Bright, W. Zhang, J. Zhang, and Y. C. Lee, “Self-aligned assembly of microlens arrays with micromirrors,” *Proc. SPIE*, vol. 3878, pp. 90–100, 1999.

[21] G. D. J. Su, J. Duparre, L. Fan, P. K. C. Wang, and M. C. Wu, “Micromachined tip-tilt micromirror array with large strokes,” *Proc. MOEMS*, pp. 39–43, 1999.

[22] J. Marshall, M. Gaitan, M. Zaghloul, D. Novotny, V. Tyree, J. I. Pi, C. Pina, and W. Hansford, “Realizing suspended structures on chips fabricated by CMOS foundry processes through the MOSIS service,” in *NISTIR 5402*, 1994.

[23] J. Soderkvist, “Similarities between piezoelectric, thermal and other internal means of exciting vibrations,” *J. Micromechanics and Microengineering*, vol. 3, pp. 24–31, 1993.

[24] W. H. Chu, M. Mehregany, and R. L. Mullen, “Analysis of tip deflection and force of a bimetallic cantilever microactuator,” *J. Micromechanics and Microengineering*, vol. 3, pp. 4–7, 1993.

[25] B. C. Read, V. M. Bright, and J. H. Comtois, “Mechanical and optical characterization of thermal microactuators fabricated in a CMOS process,” *Proc. SPIE*, vol. 2642, pp. 22–32, 1995.

[26] *MARC: MENTAT User’s Guide*. Palo Alto, CA: Analysis Research Corporation, 1994.

[27] A. Tuantranont, V. M. Bright, L. A. Liew, W. Zhang, and Y. C. Lee, “Phase-only micromirror array fabricated by standard CMOS process,” *Sensors and Actuators A: Physical*, vol. 89, no. 1–2, pp. 124–134, 2001.

[28] ——, “Smart phase-only micromirror array fabricated by standard CMOS process,” *Proc. IEEE MEMS*, pp. 455–460, 2000.

[29] W. Zhang, K. F. Harsh, M. A. Michalicek, V. M. Bright, and Y. C. Lee, “Flip-chip assembly for RF and optical MEMS,” in *Proc. ASME InterPack’99*, vol. EEP-26-1, 1999, pp. 349–354.

[30] A. Tuantranont, L. A. Liew, V. M. Bright, J. L. Zhang, W. Zhang, and Y. C. Lee, "Bulk-etched surface micromachined and flip-chip integrated micromirror array for infrared applications," *Proc. IEEE Optical MEMS*, pp. 71–72, 2000.

Adisorn Tuantranont received the B.S. degree in electrical engineering from King Mongkut's Institute of Technology Ladkrabang (KMITL), Bangkok, Thailand, in 1995, and the M.S. and Ph.D. degrees in electrical engineering (Lasers and Optics) from University of Colorado at Boulder in 1998 and 2001, respectively.

He is working in Optoelectronic Computing Systems Center (OCS) and Center for Advanced Manufacturing and Packaging of Microwave, Optical, and Digital Electronics (CAMPmode). His current research interests include MEM-deformable micromirror for optical beam steering and shaping, MEM-controllable microlens array for optical interconnect and optical communication, and micromirror for laser resonator and high power applications. He received Royal Thai Government Scholarship from 1996–2001. He has authored and co-authored more than 20 papers on optical MEMS and holds two patents on MEMS switching and fixing for optical fiber coupling and MEMS micromirrors.

Victor M. Bright received the B.S.E.E. degree from the University of Colorado at Denver in 1986, and the M.S. and Ph.D. degrees from the Georgia Institute of Technology, in 1989 and 1992, respectively.

He is an Associate Professor of Mechanical Engineering and the Director of the MEMS Research and Development Laboratory, University of Colorado, Boulder, CO. Prior to joining the University, he was an Associate Professor and the Director of Microelectronics Research Laboratory in the Department of Electrical and Computer Engineering, Air Force Institute of Technology, Wright–Patterson Air Force Base, Ohio (6/1992–12/1997). His research includes MEMS, silicon micromachining, MEMS packaging, and optoelectronics. Since 1995, he conducted an AFOSR funded effort into the development of MEMS for optical aberration control. The research resulted in the first successful demonstration of wave front aberration control using a segmented 127-element piston type micromirror array. The results of this work were published in a special issue of Optical Engineering (May 1997). Dr. Bright also conducted US Air Force sponsored research in multichip module (MCM) packaging of MEMS. This work resulted in the first reported successful packaging of MEMS in commercial MCM packages including ceramic MCM-D, High Density Interconnect (HDI), and Chip on Flex. He has authored and co-authored more than 70 papers on MEMS. He serves on the Executive Committee of ASME MEMS Sub-division and on the Technical Program Committee of the IEEE MEMS Annual Conference. He received the following awards: 1) Best Paper of the MCM'98—Intl. Conference and Exhibition on Multichip Modules and High Density Packaging, Denver, CO, April 15–17, 1998; 2) Best Paper of Session—International Conference and Exhibition on Multichip Modules and High Density Packaging, Denver, CO, April 15–17, 1998; and 3) R.F. Bunshah Best Paper Award—1996 International Conference on Metallurgical Coatings and Thin Films.